









# Cryo-EM structures elucidate the multiligand receptor nature of megalin

Sawako Goto<sup>a,1</sup> , Akihisa Tsutsumi<sup>b,1,2</sup>, Yongchan Lee<sup>c</sup> , Michihiro Hosojima<sup>d</sup> , Hideyuki Kabasawa<sup>d</sup>, Koichi Komochi<sup>d</sup> , Satoru Nagatoishi<sup>e</sup>, Kazuya Takemoto<sup>a</sup> , Kouhei Tsumoto<sup>f</sup>, Tomohiro Nishizawa<sup>c,3</sup>, Masahide Kikkawa<sup>b,3</sup>, and Akihiko Saito<sup>a,3</sup> 

Edited by K. Garcia, Stanford University, Stanford, CA; received October 30, 2023; accepted April 19, 2024

Megalyn (low-density lipoprotein receptor-related protein 2) is a giant glycoprotein of about 600 kDa, mediating the endocytosis of more than 60 ligands, including those of proteins, peptides, and drug compounds [S. Goto, M. Hosojima, H. Kabasawa, A. Saito, *Int. J. Biochem. Cell Biol.* **157**, 106393 (2023)]. It is expressed predominantly in renal proximal tubule epithelial cells, as well as in the brain, lungs, eyes, inner ear, thyroid gland, and placenta. Megalyn is also known to mediate the endocytosis of toxic compounds, particularly those that cause renal and hearing disorders [Y. Hori *et al.*, *J. Am. Soc. Nephrol.* **28**, 1783–1791 (2017)]. Genetic megalyn deficiency causes Donnai–Barrow syndrome/facio-oculo-acoustico-renal syndrome in humans. However, it is not known how megalyn interacts with such a wide variety of ligands and plays pathological roles in various organs. In this study, we elucidated the dimeric architecture of megalyn, purified from rat kidneys, using cryoelectron microscopy. The maps revealed the densities of endogenous ligands bound to various regions throughout the dimer, elucidating the multiligand receptor nature of megalyn. We also determined the structure of megalyn in complex with receptor-associated protein, a molecular chaperone for megalyn. The results will facilitate further studies on the pathophysiology of megalyn-dependent multiligand endocytic pathways in multiple organs and will also be useful for the development of megalyn-targeted drugs for renal and hearing disorders, Alzheimer's disease [B. V. Zlokovic *et al.*, *Proc. Natl. Acad. Sci. U.S.A.* **93**, 4229–4234 (1996)], and other illnesses.

cryoelectron microscopy | endocytosis | ligand binding | megalyn | proximal tubule

Endocytosis is a vital cellular process involved in nutrient uptake, intercellular signaling, membrane recycling, and pathogen infection. Receptor-mediated endocytosis is generally initiated by ligand binding to endocytic receptors on the cellular surface (1, 2). A variety of endocytic receptors have been identified, including those belonging to the low-density lipoprotein receptor (LDLR) family (3). LDLR family members play important roles in molecular uptake and transport in various types of cells and they possess common structural elements including complement-type repeats (CRs), epidermal growth factor (EGF)-type repeats (EGFRs), and the  $\beta$ -propellers that contain tyrosine-tryptophan-threonine-aspartic acid (YWTD) motifs. However, the domain composition varies among members and can be roughly classified into small, large, and giant classes, mainly according to the number of  $\beta$ -propellers (3) (*SI Appendix, Extended Data Fig. 1*).

LDLR-related protein 2 (LRP2), commonly known as megalyn, is a giant (~600 kDa) glycoprotein member of the LDLR family (4), whose homolog is found even in *Caenorhabditis elegans* (5). Megalyn consists of a large N-terminal extracellular region, a single transmembrane (TM) segment, and a short C-terminal cytoplasmic domain (4). The extracellular region contains four putative functional domains, called the ligand-binding domains (LBD) I to IV, which consist of CR clusters, and eight YWTD  $\beta$ -propellers (3, 4). Megalyn mediates the uptake of a variety of ligands (more than 60), including vitamin-carrier proteins, peptide hormones, and drug compounds (2, 6).

In mammals, megalyn is predominantly expressed at the apical membrane of renal proximal tubule epithelial cells (7), where it mediates the reabsorption of glomerular-filtered proteins, peptides, and essential substances to prevent their loss in the urine. Megalyn is also expressed in the epithelial cells of other organs, including the brain, lungs, placenta, eyes, inner ear, and thyroid gland (8). Mutations of the megalyn gene (*LRP2*) cause Donnai–Barrow syndrome/facio-oculo-acoustico-renal syndrome in humans that is characterized by malformation of forebrain and facial structures, ocular and hearing disorders, and urinary loss of megalyn ligands (9). Megalyn is also known to mediate proximal tubular endocytosis of nephrotoxic antimicrobials as well as anticancer agents such as gentamicin, vancomycin, colistin, and cisplatin, thereby causing drug-induced kidney injury (10). Some of these nephrotoxic drugs also exhibit ototoxicity, which is likely mediated by

## Significance

Megalyn (low-density lipoprotein receptor-related protein 2) is a giant endocytic receptor predominantly expressed at the apical membrane of renal proximal tubule epithelial cells. It internalizes ligands of proteins and peptides as well as toxic drug compounds that cause cell injury. However, how megalyn associates with a wide variety of ligands remains unknown. Here, we elucidated the dimeric architecture of megalyn, purified from rat kidneys, using cryoelectron microscopy. The maps revealed the densities of endogenous ligands bound to various regions throughout the dimer, elucidating the multiligand receptor nature of megalyn. We also determined the structure of megalyn in complex with receptor-associated protein, a molecular chaperone for megalyn. The results will facilitate further pathophysiological studies on megalyn-mediated endocytosis and megalyn-targeted drug development.

Competing interest statement: A.S. received research grants from Denka Co., Ltd.

This article is a PNAS Direct Submission.

Copyright © 2024 the Author(s). Published by PNAS. This article is distributed under [Creative Commons Attribution-NonCommercial-NoDerivatives License 4.0 \(CC BY-NC-ND\)](https://creativecommons.org/licenses/by-nc-nd/4.0/).

<sup>1</sup>S.G. and A.T. contributed equally to this work.

<sup>2</sup>Present address: Daiichi Sankyo Co., Ltd., Tokyo 140-8710, Japan.

<sup>3</sup>To whom correspondence may be addressed. Email: t-2438@yokohama-cu.ac.jp, mkikkawa@m.u-tokyo.ac.jp, or akisaito@med.niigata-u.ac.jp.

This article contains supporting information online at <https://www.pnas.org/lookup/suppl/doi:10.1073/pnas.2318859121/-/DCSupplemental>.

Published May 21, 2024.

megalín. Therefore, megalín is of particular interest in the development of reno- and otoprotective drugs. For example, cilastatin was identified as a megalín blocker for reno- and otoprotective effects against nephro- and ototoxic substances (10, 11). The putative involvement of megalín in the pathogenesis of Alzheimer's disease (12) also raises hopes for the development of drugs targeting the disease.

Most recently, Beenken et al. reported cryoelectron microscopy (cryo-EM) structures of mouse megalín under neutral and low pH conditions, revealing a pH-dependent structural change (13). However, the mechanism by which megalín associates with such a wide variety of ligands is not known. Structural studies have thus far been limited to the NMR studies of the interaction of specific CRs with gentamicin (14). Similar to other LDLR family members (15, 16), megalín is bound in the endoplasmic reticulum (ER) by receptor-associated protein (RAP), which is a molecular chaperone that facilitates proper folding and membrane trafficking of megalín (17, 18). Upon binding its ligands at the cell surface, megalín is internalized in early endosomes; it then releases its ligands and is recycled to the cell surface (19, 20). Megalín–ligand dissociation is thought to be associated with decreases in pH and  $\text{Ca}^{2+}$  concentration in endosomes (19), but it remains unclear how RAP and other ligands associate with and dissociate from megalín.

Here, we report the cryo-EM structures of rat megalín, purified from kidneys, with and without its molecular chaperone RAP. These structures reveal that megalín constitutes a giant dimeric architecture forming a unique bird-shaped domain organization. The cryo-EM maps further reveal that endogenous ligands bind to various regions throughout the dimer, explaining the multiligand receptor nature of megalín, which is probably shared by related receptors such as LRP1.

## Results

**Structure Determination of Megalín.** Megalín was purified from the brush border-enriched fraction of rat kidneys by using the anti-megalín monoclonal IgG-coupled affinity column and size-exclusion chromatography (SEC) (*Materials and Methods* and *SI Appendix, Extended Data Fig. 2 A–C*). Fractionated megalín proteins were evaluated by blue native polyacrylamide gel electrophoresis (BN-PAGE), which estimated the size of megalín as being larger than 1,048 kDa. This estimated size suggested that most of the purified megalín was dimerized, given that its calculated molecular mass is about 600 kDa (*SI Appendix, Extended Data Fig. 2C*). Immunoblotting of rat kidney cortex lysates, separated by BN-PAGE and stained with an anti-megalín antibody, also indicated that the molecular mass was greater than 1,048 kDa (*SI Appendix, Extended Data Fig. 2D*), suggesting that native megalín in the kidney is also present in the dimeric form.

The purified megalín was vitrified and subjected to cryo-EM single-particle analysis (*SI Appendix, Extended Data Fig. 3 and Table S1*). The refined global map revealed the dimeric architecture of megalín, with a total mass of about 1.2 MDa, which forms complicated interaction networks between the two protomers. The megalín dimer shows a  $C2$  symmetry and has a unique bird-like shape with each protomer consisting of domains resembling a head, wing, body, and leg (Fig. 1). Since the consensus cryo-EM map showed low densities for some of the flexible regions, we performed a multibody refinement with RELION-3 for the six interconnected domains (*SI Appendix, Extended Data Fig. 3 and Table S1*). This strategy yielded maps of the individual domains better resolved, with resolutions ranging between 3.2 and 3.8 Å. Although some regions were only weakly visible in the

cryo-EM maps, almost all ectodomains were traced on the density, aided by the fragmentary prediction models generated by AlphaFold2 (21) (Fig. 1). The micelle density was weakly visible, while the TM segment and the C-terminal cytoplasmic domain were disordered (Fig. 2A) and thus not included in the model (Fig. 1A). More than 40 glycans per protomer are visualized in the cryo-EM map, consistent with the prediction from the amino acid sequence as well as mass spectroscopic studies (22). These glycans also contribute to the overall architecture of megalín (Fig. 2A).

There are several inter- and intraprotomer interactions (*SI Appendix, Extended Data Fig. 4 A–D*). The head domain forms a major dimeric interaction, accounting for about 40% (2,600 Å<sup>2</sup>) of the total interaction area (6,800 Å<sup>2</sup>), which is partially mediated through the coordinated metal cations, including  $\text{Ca}^{2+}$  and  $\text{Ni}^+$  (Fig. 2 F, I, and J). The N terminus of each protomer is adjacent to the lipid membrane and attaches to the leg domain of the other protomer near the TM segment, where the first and second CR (CR1 and CR2) in LBD I directly coordinate with the positively charged residues of the other protomer (Lys4337 and Lys4027 in  $\beta 8$  and EGFR15, respectively), consistent with the typical mode of interaction in CRs (23) (*SI Appendix, Extended Data Fig. 4 C, E, and F*). Each CR contains a  $\text{Ca}^{2+}$  binding motif consisting of carboxyl residues and backbone carbonyls stabilized by three pairs of disulfide bonds, and it provides a platform for positively charged ligands in a  $\text{Ca}^{2+}$ -dependent manner (24) (*SI Appendix, Extended Data Fig. 4 E and F*). There are additional interactions at the wing–body (*SI Appendix, Extended Data Fig. 4B*) and leg–leg domain interfaces (*SI Appendix, Extended Data Fig. 4D*), and all these interactions are likely to stabilize the overall architecture of megalín at pH 7.4.

**Endogenous Ligand Binding.** Mass spectrometric analysis of purified megalín revealed that various proteins were copurified with megalín, including known endogenous ligands such as retinol-binding protein (25) and hemoglobin (26) (*SI Appendix, Table S2*). Consistently, cryo-EM maps revealed unidentified densities in various regions throughout the dimer, indicating putative ligand-binding sites of megalín (Fig. 2 A and B). Although it has long been believed that the CR clusters (LBDs) are essentially responsible for ligand binding (27, 28), the current structure revealed that CRs and  $\beta$ -propellers together create several distinct architectures that are presumably important for ligand binding (Fig. 2 A–H).

LBD I and III are composed of CRs only and constitute flexible linker regions that connect the leg–wing and wing–body domains, respectively (Fig. 2A and *SI Appendix, Extended Data Fig. 1A*). Ligand density was observed at LBD III and is probably recognized via typical CR interactions. Although LBD I was not clearly visualized in the cryo-EM map due to flexibility, it may also have a similar role in ligand binding.

The CRs of LBD II and IV encircle the periphery of the  $\beta$ -propeller regions ( $\beta 1$ – $\beta 2$  and  $\beta 7$ , respectively), and together they constitute concave architectures, which we respectively termed  $\beta$ -basket and  $\beta$ -pocket (Fig. 2 A, B, D, and E). Strong continuous densities were observed at the center of each  $\beta$ -propeller, which are at almost the same level as in the protein part and could not be explained by the binding of solvent water or ions. Given the similarity to other YWTD  $\beta$ -propeller-containing proteins, including LRP6 (29, 30) and nidogen (31) (*SI Appendix, Extended Data Fig. 5 E–G*), it is likely that the observed density is in part derived from endogenous peptide ligands, suggesting a structural feature common among the ligands for the  $\beta$ -propellers (Fig. 3 A and B and *SI Appendix, Extended Data Fig. 5 A and B*).

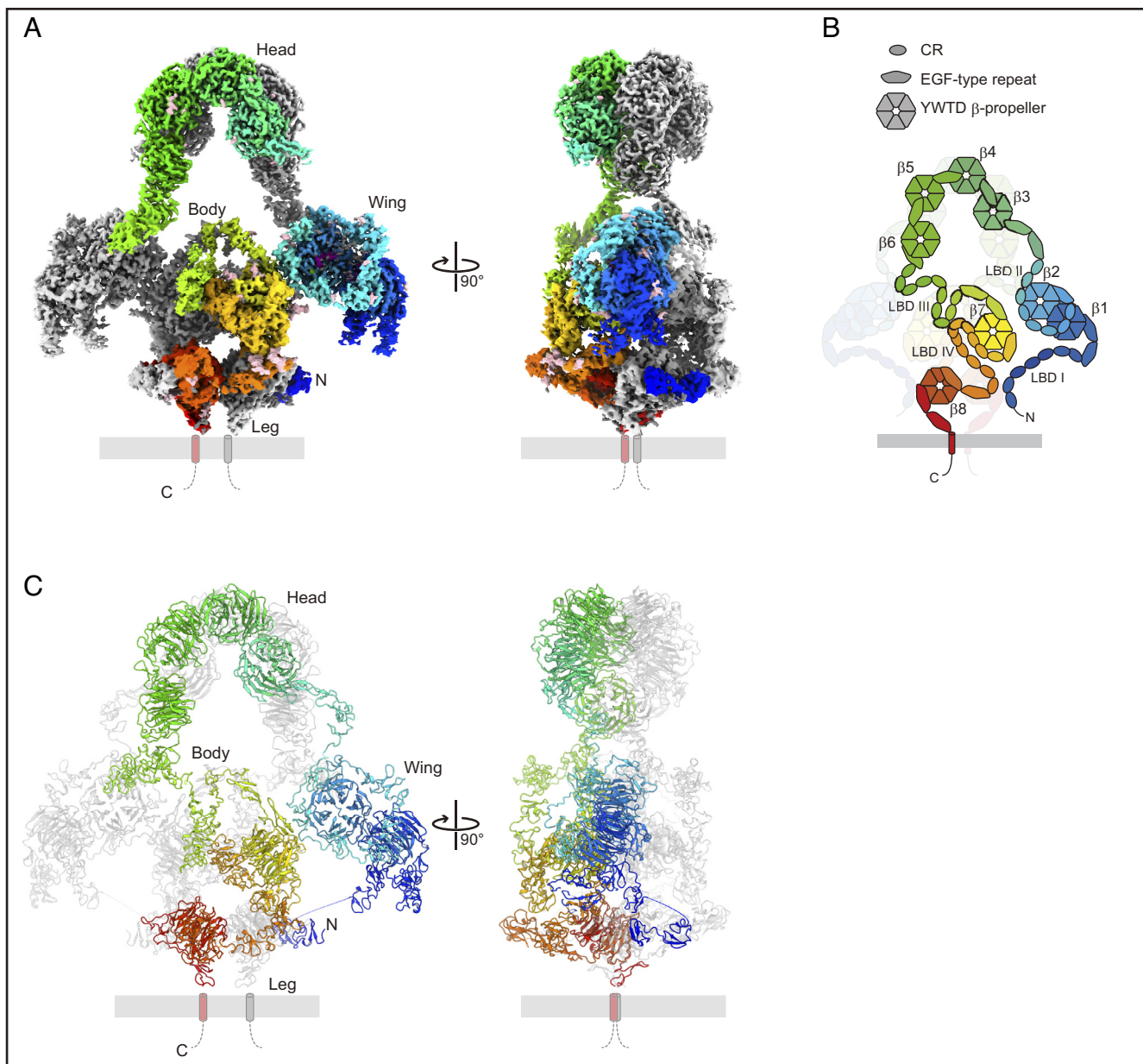


**Fig. 1.** Structure of rat megalin. (A) Cryo-EM density of overall rat megalin, viewed parallel to the membrane plane. Domains are indicated within the panel. (B) Cartoon representation of the domain composition of rat megalin. CR, EGF-type repeat, and YWTD-containing  $\beta$ -propeller are indicated by ovals, wide pentagons, and hexagons, respectively. (C) Overall structure of rat megalin shown as a ribbon model. One of the protomers is shown in rainbow colors, while the other is shown in gray or is transparent.

The peptide-bond moieties of the putative ligands are recognized by the pairs of Glu/Asp–Arg residues, which are located in the third and fourth blades, respectively (Glu469–Arg512 in  $\beta 1$ , Glu786–Arg826 in  $\beta 2$ , and Glu3275–Arg3324 in  $\beta 7$ ), and are highly conserved among the  $\beta$ -propellers (Fig. 3). In  $\beta 2$  and  $\beta 7$ , additional Asn residues (Asn872 and Asn3370, respectively) in the fifth blade form hydrogen-bond interactions with the side-chain moiety of the ligands. Therefore, this type of interaction is likely to be conserved among YWTD  $\beta$ -propeller-containing proteins. Overall, ligand recognition in the  $\beta$ -pocket and  $\beta$ -basket is mediated by the combination of two types of interactions; that is, the YWTD  $\beta$ -propellers bind to the unstructured peptides or protein loops, and the surrounding CRs bind to the positive charges of the ligand surface. Among the eight YWTD  $\beta$ -propellers in megalin, no ligand density was observed at  $\beta 8$  in the leg domain, which lacks the pairs of Glu/Asp–Arg residues (Fig. 3C and

*SI Appendix, Extended Data Fig. 5C*), indicating that  $\beta 8$  is not involved in ligand recognition.

The head domain consists of a pair of four  $\beta$ -propellers ( $\beta 3$ – $\beta 6$ ) from the two protomers. This region does not contain any CR sequences and thus has not been considered as a ligand-binding site, but ligand densities were observed in the central “ $\beta$ -cage” surrounded by the  $\beta$ -propellers, which we termed the “ $\beta$ -cage” (Fig. 2A–C and *SI Appendix, Extended Data Fig. 5D*). Similar to the  $\beta$ -pocket and  $\beta$ -basket, polypeptide-like densities were observed at the center of the  $\beta$ -propellers in the  $\beta$ -cage, but the ligand preference seems to vary among the  $\beta$ -propellers (Fig. 3D).  $\beta 3$  and  $\beta 6$  have the consensus motif of Glu/Asp–Arg and recognize the peptide backbone of the ligands in a similar manner.  $\beta 6$  has an additional Asn residue (Asn2555) in the fifth blade and it seems to interact with the hydrophilic side-chain moiety of the ligands, as observed in similar  $\beta$ -propeller proteins (*SI Appendix, Extended Data Fig. 5E–G*).

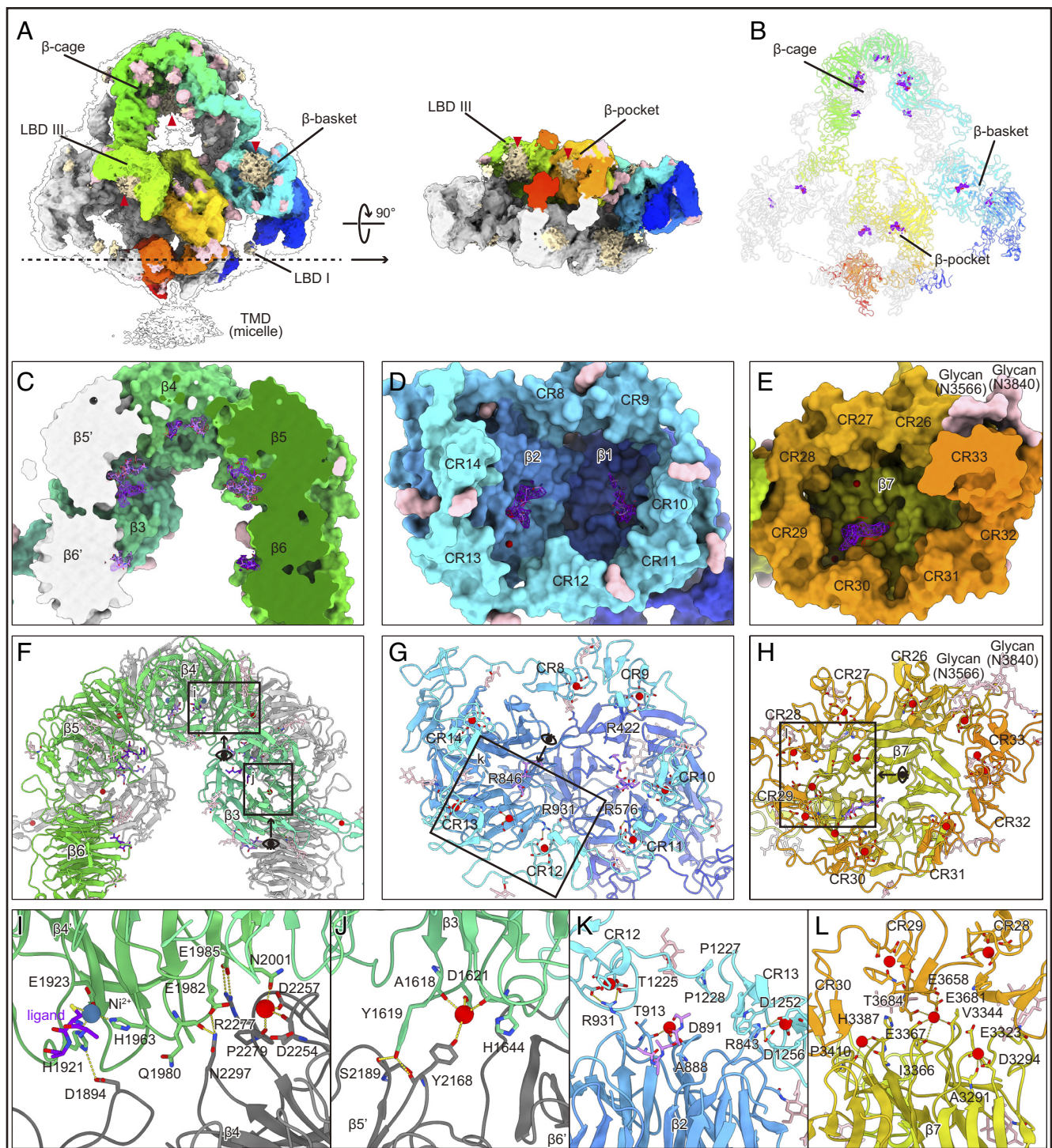


**Fig. 2.** Ligand-binding sites of megalin. (A) Unsharpened cryo-EM density of rat megalin viewed parallel to the membrane plane (*Left*) and a cutaway surface of the density at the dotted line viewed from the cytoplasmic side (*Right*). Density is shown for the low- (transparent) and high-contoured (colored) areas in the *Left* panel, and the low-contoured map shows the micelle density of the TM domain (TMD). The colors correspond to those in Fig. 1, with O- and N-glycans highlighted in pink. Extra densities of endogenous ligands are indicated by red arrowheads. The ligand densities are observed at the binding sites indicated in the panels, except for LBD I, whose density is rather weak and indicated in the middle of the CRs. (B) *Fo-Fc* densities of ligand-binding sites are highlighted in purple, showing the extra strong density of endogenous ligands. Rat megalin is shown as a ribbon model. (C–E) Surface representations are shown for the head domain (C),  $\beta$ -basket (D), and  $\beta$ -pocket (E).  $\beta$ -propellers and CRs are indicated. Positive and negative *Fo-Fc* density maps are shown in purple and red, respectively. A probable architecture of protein ligands is shown as purple sticks. Two N-glycans on the CRs of  $\beta$ -pocket are indicated in E. (F–H) Ribbon models are shown for the head domain (F),  $\beta$ -basket (G), and  $\beta$ -pocket (H).  $\text{Ca}^{2+}$  ions are indicated by red spheres. O-glycans are predominantly present on the spacer regions of CRs but are on the opposite sides in the  $\beta$ -basket (G) and  $\beta$ -pocket (H). The *insets* show the zoomed-in region of (I and J), with the viewpoints indicated by the eye symbols. (I–L) Zoomed-in views showing the interactions within the ligand-binding sites for the head domain (I and J),  $\beta$ -basket (K), and  $\beta$ -pocket (L). Hydrogen-bond interactions are indicated by yellow dotted lines.

$\beta 5$  has several basic residues—Arg2149, Arg2194, Arg2238, Arg2296, and Arg2325—and the elongated density of the ligand side chain suggests that these residues preferentially interact with

the negatively charged Asp and Glu residues of the ligands.  $\beta 4$  also has a unique interaction mode, in which the putative ligand and His1921, His1963, and Glu1923 coordinate a sphere density that

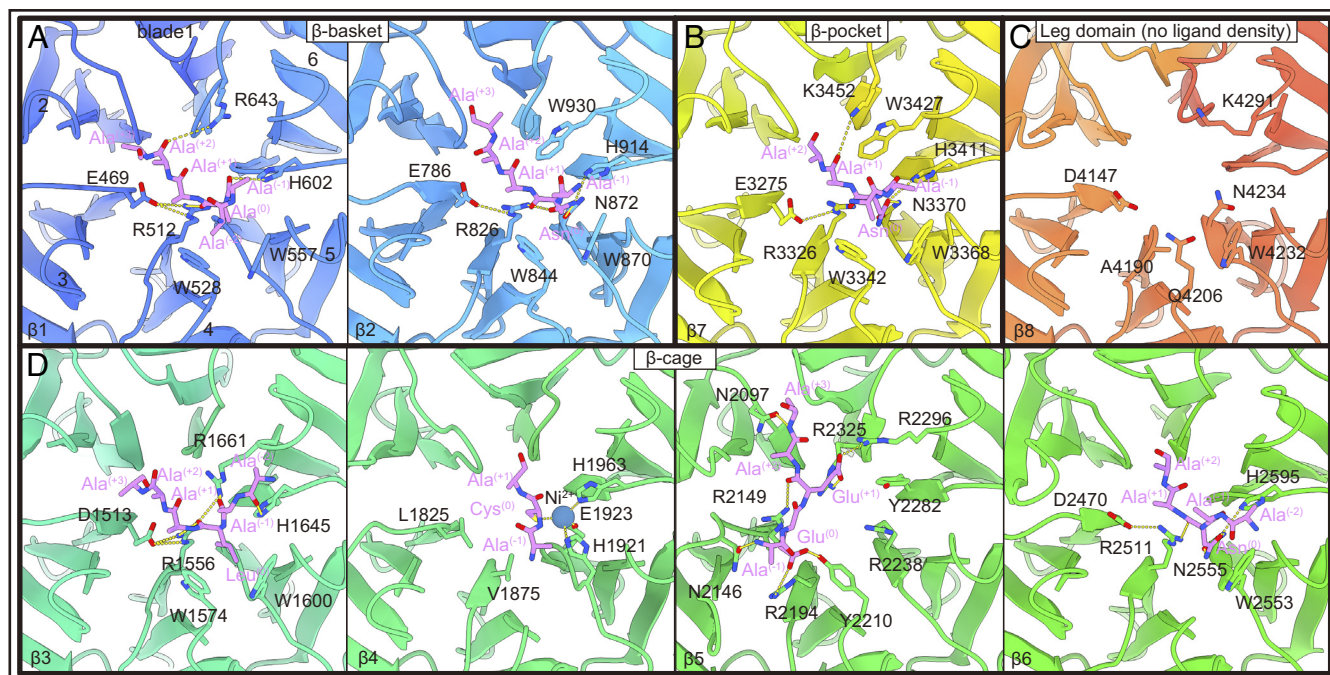


**Fig. 3.** Binding of peptide ligands in  $\beta$ -propellers. (A–D) Zoomed-in views of the  $\beta$ -propellers are shown for the  $\beta$ -basket (A),  $\beta$ -pocket (B), the leg domain (C), and the head domain (D).  $\beta$ -propeller numbers ( $\beta 1$ – $\beta 8$ ) are shown in the *Lower Left* corner, and blade numbers are indicated in the *Upper Left* panel ( $\beta 1$ ). Colors are the same as those in Fig. 1. Possible architectures of peptide ligands are shown as light purple sticks.  $\beta$ -propeller residues important for ligand recognition are shown as sticks. A pair of Asp/Glu–Arg residues, on the third and fourth blades, respectively, are conserved in  $\beta 1$ – $\beta 3$ ,  $\beta 6$ , and  $\beta 7$ , whereas  $\beta 4$  and  $\beta 5$  have different motifs for ligand recognition. Amino acid residues of the ligands are assigned based on the density shapes and the similarity to the previous ligand-bound structures of the YWTD-containing  $\beta$ -propellers (*SI Appendix, Extended Data Fig. 5 A–C*), while densities with fewer features are assigned as Ala. The residue number of the ligands is defined such that the residues recognized by the conserved motifs (e.g., Asn in  $\beta 2$ ) are zero.

most likely represents a metal ion (Fig. 3D). We assigned  $\text{Ni}^+$  to this metal ion density based on the coordination geometry, and this suggests that  $\beta 4$  prefers ligands containing metal-coordinating residues, such as Cys, His, Met, Asp, and Glu, as well as other small compounds that can bind to the metal ions. Overall, the  $\beta$ -cage can recognize a variety of ligands that can be accommodated within the cage, which is approximately 30 to 40 Å in width, by the combination of the eight  $\beta$ -propellers with various preferences. The distinct forms of ligand-binding sites, including the CRs (LBD I and III),  $\beta$ -pocket,  $\beta$ -basket, and  $\beta$ -cage, explain the multiligand receptor function of megalin. Most notably, the ligand binding in each site is supported by the coordination of weak, nonspecific recognition by the multiple structural modules. Such interaction enables megalin to recognize a wide range of ligands.

Several surface glycans are found in the ligand-binding sites of megalin. Two *N*-glycans attached to Asn3566 and Asn3840 in CR26 and CR33, respectively, are located in a close proximity, stabilizing the circular arrangement of CRs in the  $\beta$ -pocket (Fig. 2 E and H). *O*-glycans are predominantly located in the spacer regions between the CRs of the  $\beta$ -pocket and  $\beta$ -basket (Fig. 2 D, E, G, and H), and some of the core *N*-acetylgalactosamines attached to Thr/Ser residues are in contact with the Pro residue(s) in the neighboring CRs (e.g., the *O*-glycan of Thr1225 in contact with Pro1227 and Pro1228 in Fig. 2K), likely stabilizing the circular arrangement of CRs around the  $\beta$ -propellers in the  $\beta$ -pocket and  $\beta$ -basket (Fig. 2 G and H). *O*-glycans are also present in CRs in LBD I and III (32), although the cryo-EM density of these glycans is not visualized due to the flexibility in these regions. Previous studies have shown that *O*-glycans are important for both protein folding and ligand interaction in megalin and other LDLR family members (32, 33). Therefore, *N*- and *O*-glycans are likely to contribute to the integrity of the ligand-binding sites and to facilitate the ligand interaction of megalin.

**Structure of Megalin in Complex with RAP.** RAP resides in the ER and facilitates folding and membrane trafficking of megalin (34). Megalin–RAP complexes are also found at the surface of some cells, including rat glomerular epithelial cells, and undergo endocytic trafficking (34). RAP has been regarded as the model ligand of megalin and other LDLR family members because it competes with the binding of various ligands to the receptors (35–37). To elucidate how megalin binds to RAP, we investigated the cryo-EM structure of megalin in complex with RAP. Purified megalin was mixed with recombinant rat RAP at neutral pH, and the complex fraction was separated from the excess RAP by using SEC and then subjected to cryo-EM analysis (*SI Appendix, Extended Data Figs. 6 and 7*). Two extra densities of the  $\alpha$ -helical bundle were observed at LBD I and LBD III (*SI Appendix, Extended Data Fig. 8A*). RAP comprises domains 1 to 3 (D1 to D3), with each domain consisting of a three-helix bundle (*SI Appendix, Extended Data Fig. 8*). The density at LBD III is consistent with the D1 domain, which has shorter helices compared to D2 and D3 (*SI Appendix, Extended Data Fig. 8A*). Despite its moderate local resolution (5 to 7 Å) (*SI Appendix, Extended Data Fig. 7E*), the asymmetric shape of the three helical bundle allowed reasonable fitting to the density. The density at LBD I is more clearly resolved (3.5 to 6 Å) and sufficient to identify it as the D3 domain (*SI Appendix, Extended Data Fig. 9B*). Altogether, the cryo-EM map indicated a 2:2 heterotetramer complex formation of megalin with RAP (Fig. 4A and *SI Appendix, Table S3*). D1 and D3 respectively bind to LBD III and LBD I from the two protomers, whereas D2 is only slightly visible as a density blob between D1 and D3 in the consensus map and has no interaction with megalin (Fig. 4 A–C and *SI Appendix, Extended Data Fig. 9A*). Megalin–RAP interaction is likely to be mediated via the typical CR interaction mode between the positively charged residues of RAP and the  $\text{Ca}^{2+}$ -chelating motifs of CRs, consistent with the  $\text{Ca}^{2+}$ -dependence

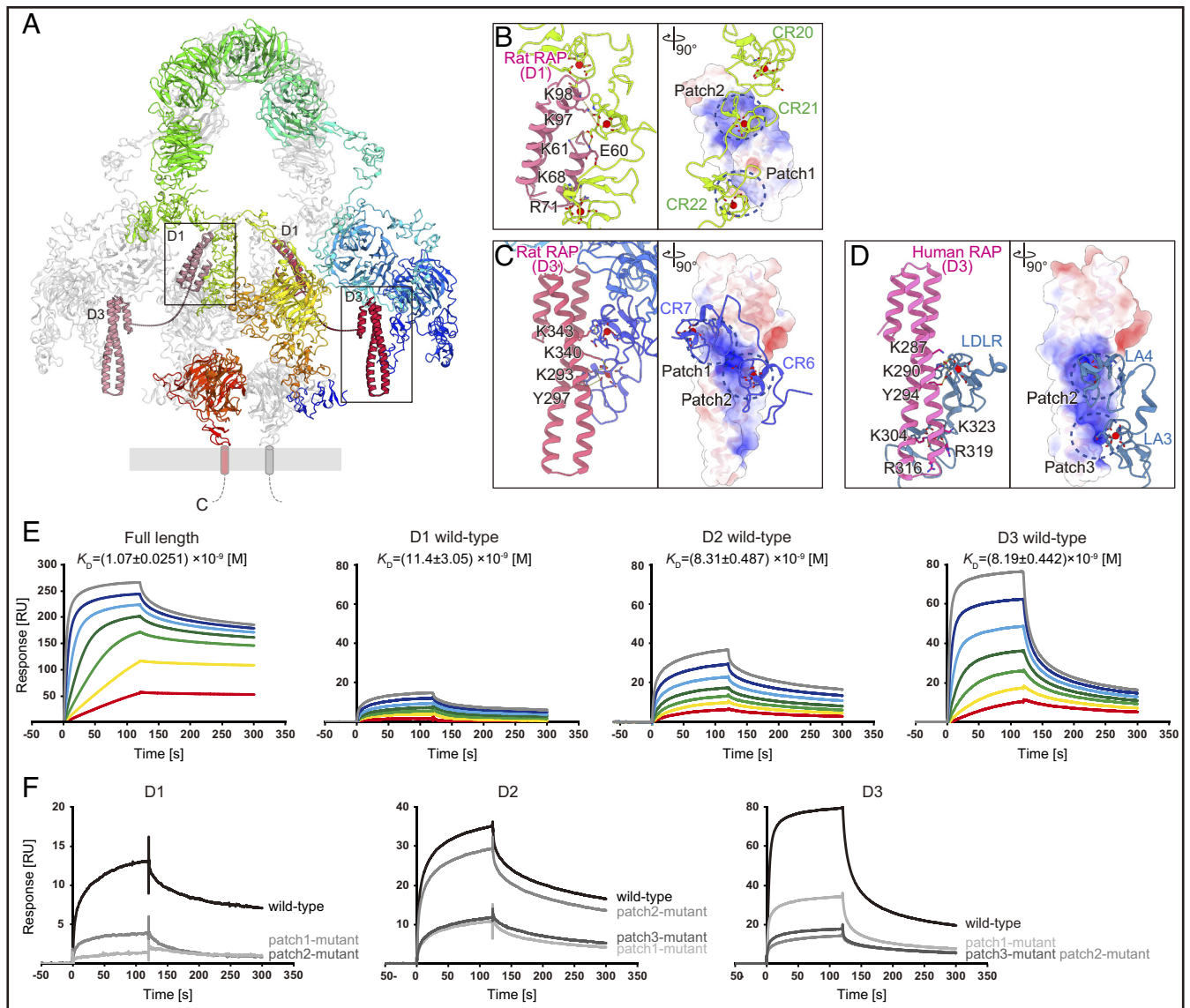


**Fig. 4.** Structure of rat megalin in complex with RAP. (A) Overall structure of rat megalin–RAP complex shown as ribbon models. The megalin color codes are the same as those in Fig. 1, while RAP is shown in red. Two protomers of RAP bind to the megalin dimer, with each protomer bridging two protomers of megalin. Insets indicate the zoomed-in regions in (B and C). (B–D) Zoomed-in views of the megalin–RAP complex of rat RAP D1 (B) and D3 (C) in the present structure, and human RAP D3 in complex with CRs (LA3–4) of LDLR (PDB: 2FCW) (D). Residues involved in the interactions are shown as sticks (Left). Right panels show the surface electrostatic potentials of the RAP domains, viewed from a perpendicular angle relative to the Left panels. Positively charged patches are highlighted as blue dotted circles. Complex formation is mediated through different patches of RAP in the two structures. Residue number is not consistent between human and rat RAP (SI Appendix, Extended Data Fig. 8A). (E) Surface plasmon resonance (SPR) response curves are shown for the interaction of full-length as well as wild-type forms of D1, D2, and D3 of RAP with megalin immobilized on a sensor. Line colors indicate the concentration of the analyte proteins (a twofold dilution series starting at 200 nM [gray], with seven points of concentration change [red: lowest]). The average value of the dissociation constant ( $K_D$ ) with the SD is shown in each panel. (F) SPR response curves are shown for the interaction of wild-type as well as patch mutant forms of each domain with megalin immobilized on a sensor. The concentration of the analyte proteins was 200 nM. Representative sensorgrams are shown from multiple experiments ( $n = 4$ ; E and F).

of the RAP association (17, 38) (Fig. 4 B–D and SI Appendix, Extended Data Fig. 4F). D1 has two positively charged patches, which are recognized by CR21 and CR22 of megalin LBD III, respectively (Fig. 4B and SI Appendix, Extended Data Fig. 8A). D3 has three patches, but only patch1 and patch2 are recognized by CR6 and CR7 of megalin LBD I, respectively (Fig. 4C). This similarity in interaction was also reported for the structure of the LDLR–RAP complex, but the structural comparison revealed that RAP D3 provides different patches for LDLR and megalin (Fig. 4 C and D and SI Appendix, Extended Data Fig. 8 A and E). RAP has several positively charged patches (SI Appendix, Extended Data Fig. 8A) and can probably provide variable interfaces for LDLR family members. Consistently, surface plasmon resonance (SPR) analysis indicated that each RAP domain (D1 to D3) can

bind to megalin with similar affinity (Fig. 4E). We also mutated positively charged patches on each domain and conducted SPR experiments (Fig. 4F and SI Appendix, Table S4). All the tested mutants showed reduction in the binding to megalin, indicating that each positively charged patch, including those not involved in the current megalin–RAP complex structure, contributes to the association with megalin. Therefore, it seems that RAP interacts with most of the surface CRs of megalin and other LDLR family members in a similar manner, while the interaction of a single CR with RAP is very weak and does not hold in a stable manner. The current complex structure likely reflects just one of the possible interaction modes between RAP and megalin. Such a flexible interaction may facilitate protein folding and maturation in LDLR family members in the ER, avoiding premature binding

of cellular ligands to CRs, as has been proposed for LRP1 (39). RAP is known to compete with the binding of various ligands to members of the LDLR family (35–37, 39). Although the ligand-binding sites composed only of CRs—LBD I and LBD III—are occupied by RAP, endogenous ligand densities were similarly observed in other ligand-binding sites even in the RAP-bound structure (*SI Appendix, Extended Data Fig. 9*), indicating that the competitive binding of RAP to CRs is not sufficient to release all endogenous ligands. In particular, ligands of the  $\beta$ -propellers are presumably not affected by RAP binding, given that RAP does not interact with  $\beta$ -propellers. These structures would challenge the conventional view of competition between RAP and other ligands in binding to megalin, and thus further characterization of ligand interaction will advance our understanding of the mechanism underlying megalin-mediated multiligand endocytosis.

## Discussion

In this study, we reported the cryo-EM structures of megalin purified from rat kidneys and the complex of megalin with RAP. The structures revealed the giant dimeric architecture of megalin as well as the endogenous ligand-binding sites, consisting of two different structural modules, YWTD  $\beta$ -propellers and CRs (Fig. 5). Most notably, the cryo-EM densities of the endogenous ligands have revealed that seven of the eight  $\beta$ -propellers ( $\beta 1$  to  $\beta 7$ ) are involved in the endogenous ligand binding, whereas  $\beta 8$  lacks the consensus motif for backbone recognition (Asp/Glu–Arg pair) and is unlikely to be involved in ligand binding.  $\beta$ -propellers preferentially recognize the peptide backbone of unstructured protein regions, except for  $\beta 4$  and  $\beta 5$ , which also lack the consensus motif. Instead,  $\beta 4$  has a  $\text{Ni}^{2+}$ -chelating motif and exhibits a metal-mediated interaction, whereas  $\beta 5$  is rich in positively charged residues and exhibits ionic interactions. As expected from previous studies, CRs recognize positively charged ligands, including the basic amino acids (Lys, Arg, and His) of the protein surface as well as cationic compounds. The combination of the two modules enables the formation of diverse ligand-binding sites, namely, the  $\beta$ -cage,  $\beta$ -pocket, and  $\beta$ -basket, as well as the conventional LBDs (LBD I and III), all of which have different ligand

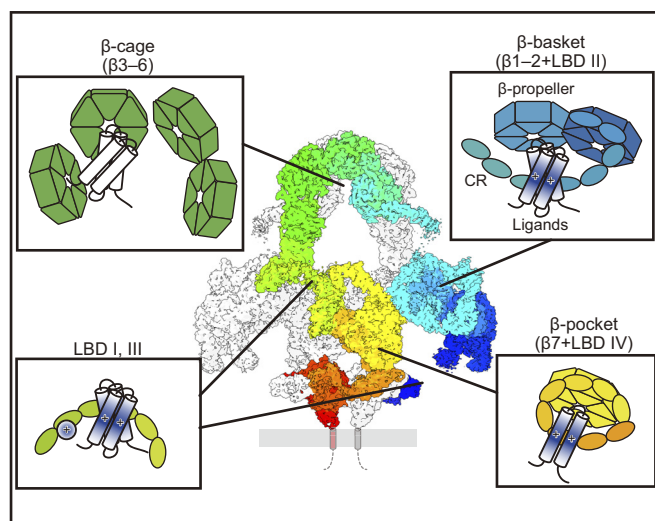


**Fig. 5.** Schematic model of ligand binding in megalin. Proposed model of the ligand interaction is shown for the  $\beta$ -pocket and  $\beta$ -basket, LBD I and III, and the  $\beta$ -cage. The ligand-binding sites consist of CRs and  $\beta$ -propellers, and ligand preference is likely dependent on the constituent modules. Ligand size may be limited by the space of each ligand-binding mode.

preferences. Physiological ligands of megalin vary in size and shape and may bind to these sites, depending on their properties (Fig. 5). For example, short peptides containing basic residues such as parathyroid hormones (40) and angiotensin peptides (41, 42) may be recognized by both  $\beta$ -propellers and CRs and thus may be accommodated in the  $\beta$ -pocket and  $\beta$ -basket, whereas small cationic compounds, including aminoglycosides such as gentamicin, may be directly recognized by flexible CRs in a  $\text{Ca}^{2+}$ -dependent manner and thus bind to LBD I and/or LBD III. The  $\beta$ -cage has been identified as a ligand-binding site in this study, and its structural features suggested that globular proteins that can be accommodated within the internal cavity bind to this cage. Based on the structural similarity to other YWTD  $\beta$ -propeller-containing proteins, the ligand interaction in the  $\beta$ -cage is likely to be mediated through the unstructured loop regions of the ligand proteins, although unusual recognition by  $\beta 4$  and  $\beta 5$  may facilitate different interaction modes with the surface side chains of ligands, thereby enabling the recognition of diverse ligands.

The triggering of ligand dissociation is also dependent on binding modes. Most ligands of megalin dissociate in early endosomes (19, 20), probably induced by the low pH of around 6.0 and the low  $\text{Ca}^{2+}$  concentration, both of which should weaken the  $\text{Ca}^{2+}$ -mediated interaction through CRs. Such a low pH generally decreases the affinity of CRs to  $\text{Ca}^{2+}$  and weakens their ligand interactions. However, the degree to which the affinity drops can vary among CRs, and some CRs are less susceptible to the change in pH and are able to hold  $\text{Ca}^{2+}$  at a pH of 5.0 (43). Thus, the existence of an additional mechanism for pH-dependent ligand release has been proposed. Recently, the structures of mouse LRP2 at extracellular and endosomal pH (7.4 and 5.2, respectively) were reported (13), revealing a drastic pH-dependent rearrangement of LRP2. The mouse LRP2 structure under neutral pH is essentially the same as the rat megalin structure in the present study (*SI Appendix, Extended Data Fig. 10, Upper*), and similar extra ligand densities were observed in the cryo-EM maps (*SI Appendix, Extended Data Fig. 11A*). The structural comparison suggests that the ligand-binding sites identified in the present study undergo rearrangement upon a decrease in pH (*SI Appendix, Extended Data Fig. 10*), and this process involves the disassembly of inter-domain interactions, including metal-mediated interactions between the  $\beta$ -propellers in the head domain (Fig. 2 *I* and *J*) and the attachment of CRs to the  $\beta$ -propellers (Fig. 2 *K* and *L*). It is worth noting that the interaction of megalin is supported by multiple structural modules, especially for large protein ligands. The pH-dependent rearrangement of megalin may prevent such cooperative ligand holding, resulting in a large decrease in the affinity of the ligands, including CR-independent ligands in the  $\beta$ -cage. In good agreement, the ligand densities were not observed in mouse LRP2 under low pH conditions (*SI Appendix, Extended Data Fig. 11B*). In contrast to general ligands, RAP can interact with megalin more tightly because its dissociation occurs in the late-endosome stage of the endocytic pathway (20), where the pH is 5.0–5.5 (44). The flexible association of RAP with multiple CRs revealed in the present study may explain this high-affinity binding and is likely responsible for the function of RAP as chaperone for various LDLR family members, although further studies will be required to elucidate the detailed mechanisms underlying megalin-mediated endocytosis.

Collectively, our findings regarding megalin and its complex with RAP have unveiled the interaction of this multiligand endocytic receptor system and will lead to further studies in pathophysiology, as well as drug development targeting megalin-mediated endocytosis.

## Materials and Methods

**Purification and Evaluation of Megalin from Rat Kidneys.** Megalin was isolated from rat kidneys using affinity chromatography as previously described (45). The concentrated megalin was further purified using Superose 6 Increase 10/300 GL (GE Healthcare Bio-Sciences AB, Uppsala, Sweden) with 150 mM NaCl, 20 mM Tris-HCl, 2 mM CaCl<sub>2</sub>, and 0.01% GDN (pH 7.4) and then fractionated into 0.5 mL at 0.4 mL/min using ÄKTA™ pure (GE Healthcare Bio-Sciences AB). The absorbance at 280 nm peaked at fractions B10–C2, which contained mainly megalin (the highest peak was fraction B12). Fractions B10–C1 were combined and concentrated to a final concentration of 2.6 mg/mL, using the 100 K ultrafiltration filter (Amicon® Ultra-0.5 mL, Centrifugal Filters Ultracel®-100 K; Sigma-Aldrich). When 4,000 g was reached, centrifugation was stopped and the sample was pipetted to avoid aggregation. A portion of the purified megalin protein from each gel-filtration fraction and the finally concentrated megalin was evaluated by BN-PAGE. Each 8- $\mu$ L sample of fraction as well as 1.0, 2.1, and 4.2  $\mu$ g protein of the finally concentrated megalin with 3  $\mu$ L of NativePAGE™ sample buffer (4 $\times$ ) (BN20032; Thermo Fisher Scientific) and 1  $\mu$ L of NativePAGE™ 5% G-250 Sample Additive (BN20041; Thermo Fisher Scientific) was electrophoresed using NativePAGE™ 4 to 16% Bis-Tris Gels (BN1004BOX; Thermo Fisher Scientific) for 240 min at 150 V. The gel was fixed with 40% methanol (Junsei Chemical Co., Ltd., Tokyo, Japan) and 10% acetic acid (Fujifilm Wako Pure Chemical Corporation) and then destained with 8% acetic acid (Fujifilm Wako Pure Chemical Corporation), after which the bands of megalin were evaluated. To evaluate natural megalin expressed in the kidney cortex, a 36- $\mu$ g lysate of rat kidney cortex was loaded and electrophoresed using BN-PAGE, and the gel was transferred to the polyvinylidene difluoride membrane. The megalin band was evaluated by immunoblotting as previously described (46), using mouse monoclonal anti-megalin carboxyl-terminal domain antibody (C25) at 4.4  $\mu$ g/mL (47).

**Analysis of Proteins Copurified with Megalin.** To comprehensively identify potential endogenous ligands bound to megalin, the purified megalin protein was analyzed by liquid chromatography/mass spectrometry. Specifically, 6.9  $\mu$ g of megalin protein purified as described above was separated by BN-PAGE. The band of dimerized megalin was cut out and reduced with 10 mM dithiothreitol (Fujifilm Wako Pure Chemical Corporation) and carbamidomethylated with 55 mM iodoacetamide (Fujifilm Wako Pure Chemical Corporation) and then subjected to in-gel digestion with trypsin (T6567; Sigma-Aldrich) as previously described (48) with only slight modification. Peptides of each sample were dissolved in 15  $\mu$ L 0.2% trifluoroacetic acid, and 2  $\mu$ L was injected into a nano-flow-LC (Eksigent nanoLC 415 with ekspert cHiPLC; SCIEX, Framingham, MA) coupled with a tandem mass spectrometer (TripleTOF5600+; SCIEX). Analysis was performed in duplicate under trap-and-elute mode, using the ChromeXP C18 Chip column (200  $\mu$ m  $\times$  0.5 mm) as the trap column and CromeXP C18 Chip column (75  $\mu$ m  $\times$  150 mm) as the analytical column. Mobile phases A and B were 0.1% formic acid and 0.1% formic acid in acetonitrile, respectively. Peptides were eluted with a 30-min gradient from 2 B to 32% B at 300 nL/min. MS spectra (250 ms) and 10 MS/MS spectra (100 ms each) were acquired under the data-dependent mode. The dynamic exclusion time was set at 12 s. Autocalibration using 50 fmol tryptic peptides of bovine serum albumin was performed every five samples.

Protein identification was performed using Mascot ver. 2.2.1 (Matrix Science, London, UK) as a search engine. The raw data generated by Analyst TF ver. 1.6 (Build 6211; SCIEX) were converted to generic Mascot files by MS Converter (SCIEX). All files for each sample were merged and searched against the Swissprot rat reference proteome database (9,798 sequences, 5,338,053 residues; 14 December 2022 release) under the instrument setting of ESI-QUAD-TOF. Peptide and MS/MS tolerance were set at  $\pm 20$  ppm and  $\pm 0.1$  Da, respectively. Modification settings were as follows: fixed modification, carbamidomethylation of cysteine; variable modifications, deamidated on asparagine and/or glutamine, phosphorylation on serine and/or threonine, N-terminal glutamine to pyroglutamate, N-terminal glutamate to pyroglutamate, and oxidation on methionine. A maximum of two missed cleavages was allowed. The significance threshold was set at  $P < 0.01$ , which yielded a false discovery rate of  $< 0.01$  at the peptide level for all the identification results. Only peptides with scores exceeding the "Identity threshold" were used. "Require bold red" was checked to avoid redundancy in protein identification.

For label-free quantitative MS analysis, the spectral abundance factor (SAF) was calculated by dividing the number of spectral counts for each protein by the protein length expressed as number of amino acids. Then, the SAF values were normalized by dividing by the sum of all SAFs for proteins in a sample to give the normalized SAF values which provides a measure of relative abundance and the ability to compare the abundance of proteins within a sample (49).

**Preparation of Recombinant RAP.** To prepare the full-length form of rat recombinant RAP (Uniprot ID: Q99068), the cDNA encoding the structure was amplified from rat kidney total RNA using RT-PCR with the following primers: forward primer: 5'-CTA GGA TCC CAT GGC GGC AAG TAC TCG CG-3' (containing BamH I restriction site), reverse primer: 5'-AGC CTC GAG TCA GAG CTC ATT GTG CCG AG-3' (containing Xho I restriction site). The PCR products were cloned into the BamH I-Xho I site of pGEX-6P-1 (Cytiva, Tokyo, Japan), which is designed to incorporate glutathione-S-transferase (GST) at the N-terminal of the recombinant proteins. In addition, the cDNAs encoding each domain of rat RAP (D1: aa52E-131K, D2: aa142N-250G, and D3: aa250G-360L) and their mutants (*SI Appendix, Table S4*) were synthesized and cloned between the BamH I and Xho I sites of pGEX-6P-1 by GenScript (Tokyo, Japan). The mutants were designed to replace lysine or arginine with alanine in each patch region of the domains. The plasmids were transfected into *Escherichia coli* DH5 $\alpha$  Competent Cells (Takara Bio Inc., Shiga, Japan) and protein expression was induced in accordance with the manufacturer's protocol. Cell lysates were sonicated and then centrifuged at 11,000 g for 20 min, after which the supernatant was used to prepare the GST-tagged target proteins. The proteins were purified using a Glutathione Sepharose 4B (Cytiva) and the GST tag was removed using PreScission™ Protease (Sigma-Aldrich) in accordance with the manufacturer's protocol.

**Preparation of the Megalin-RAP Complex.** To prepare the complex of megalin and RAP, 480  $\mu$ L of 1.5 mg/mL purified megalin (1.2 nmol) and 40  $\mu$ L of 8.4 mg/mL RAP (8.35 nmol) were incubated for 2 h at 4 °C in a rotary shaker and then fractionated by gel-filtration as described above. The peak fractions at B9–B12 contain the megalin-RAP complex, and the later fractions (C7–D1) contain unbound RAP. The fractions B9–B11 were mixed and concentrated to a final concentration of 2.3 mg/mL by using an ultrafiltration filter as described above. Aliquots of each fraction were evaluated by BN-PAGE. The gel-filtration fractions were also analyzed by sodium dodecyl sulfate-polyacrylamide gel electrophoresis.

**SPR Analysis.** The interactions of purified megalin with recombinant full-length rat RAP, as well as with the wild-type and mutant forms of each domain (D1, D2, and D3) of rat RAP, were analyzed based on SPR, using a Biacore T200 instrument (Cytiva). For SPR, purified megalin was fractionated by SEC with 20 mM 4-(2-hydroxyethyl)-1-piperazineethanesulfonic acid (HEPES) (pH 7.4), 150 mM NaCl, 2 mM CaCl<sub>2</sub>, and 0.01% GDN. The CM7 Biacore sensor chip (Cytiva) was activated by treatment with *N*-hydroxysuccinimide/*N*-ethyl-*N'*-(3-dimethylaminopropyl) carbodiimide hydrochloride, followed by immobilization of megalin at around 2,700 resonance units. After immobilization, the activated surface of the sensor chip was blocked with 1 M ethanolamine hydrochloride (pH 8.5). Full-length RAP, as well as the wild-type and mutant forms of D1, D2, and D3 of RAP, were injected onto the sensor chip at a flow rate of 30  $\mu$ L/min in a range of concentrations for a twofold dilution series starting at 200 nM, with 7 points of concentration changes. The association and dissociation times were 120 and 600 s, respectively. The assay was carried out in 10 mM HEPES (pH 7.5), 150 mM NaCl, and 2 mM CaCl<sub>2</sub> containing 0.005% (v/v) Tween-20 at 25 °C. A regeneration procedure was performed at the end of each cycle with 1 M arginine-HCl (pH 4.4). The data were analyzed with BIAevaluation software (Cytiva), and the average values of the dissociation constant ( $K_D$ ) with the SE were calculated by fitting the equilibrium curve, using BIAevaluation software (Cytiva).

**Cryo-EM Analysis.** The purified samples were vitrified using Vitrobot Mark IV (Thermo Fisher Scientific), and then 3.0  $\mu$ L aliquots were applied onto glow-discharged grids (Cu/Rh 1.2/1.3; Quantifoil, Großlobichau, Germany) and blotted for 4 s at a blot force of 0. For the megalin sample, the grid was pretreated by pentylamine. Data were collected using a Titan Krios microscope (Thermo Fischer Scientific) equipped with a K3 camera (Gatan) at The University of Tokyo. Automated data acquisition was performed by SerialEM (50), using beam image shift, at a nominal magnification of 105,000 (0.83 Å/pixel calibrated pixel size). A total of 4,660 movies for megalin were recorded in CDS mode, with a total dose of



50 e<sup>-</sup> Å<sup>-2</sup>, fractioned into 49 frames, although the first frame was omitted for the processing. The data were processed by RELION ver. 3.1 (51). After motion correction and contrast transfer function (CTF) estimation, particles were picked using Topaz (52) and extracted at 3.3 Å/pixel. After 2D and 3D classification, good particles were re-extracted at 1.66 Å/pixel, and 3D refinement was performed with an imposed C2 symmetry. Then CTF refinement as well as beam-tilt and aberration corrections were performed. Bayesian particle polishing was also performed, with the box and binned sizes changed to 442 and 260 pixels, respectively (resultant pixel size: 1.41 Å/pixel), after which CTF refinement was performed again. Next, 3D refinement was performed with a relaxed C2 symmetry, and the particles were subjected to multibody refinement with the five defined bodies. Resolution was estimated based on the gold-standard Fourier shell correlation. Data acquisition and processing for the megalin-RAP complex were similarly performed, with slight modifications. A total of 4,518 movies were recorded in normal mode, with a total dose of 48 e<sup>-</sup> Å<sup>-2</sup>, and then fractioned into 48 frames. Particles were picked by a Laplacian of Gaussian-based method implemented in RELION, extracted at 3.3 Å/pixel and subjected to 2D and 3D classification. Good particles were re-extracted at 1.66 Å/pixel and subjected to Refine3D with imposed C2 symmetry, Bayesian polishing, Refine3D with relaxed C2 symmetry, and multibody refinement. We generated fragmentary prediction models of megalin by using AlphaFold2; the models were manually fitted to each multibody-refined map and used as the initial template. The models were manually rebuilt in Coot (53), fitted to the density by ISOLDE (54), implemented in chimeraX (55), and refined to each multibody-refined map by using phenix.real\_space\_refine (56). The composite maps were generated by using phenix.combine\_focused\_maps (56), and the composite models were generated by fitting each model in Coot, adjusted by ISOLED, and refined to the combined map by Servalcat (57). Focused maps and models were used to show the domain structures and interactions, while the composite maps and models were used to show the overall structures of megalin and its complex with RAP. Figures were prepared by Cuemol2 (<http://www.cuemol.org/en/>) and ChimeraX (55).

**Data, Materials, and Software Availability.** The proteomics data have been deposited in the ProteomeXchange Consortium (<http://www.proteomexchange.org>) via jPOST (Japan Proteome Standard Repository/Database, <https://jpostdb.org>) with the dataset identifier PXD040563 (58). The coordinates and cryo-EM maps of rat megalin are deposited with the PDB and EMD codes of 8JUJ (59) and

EMD-36664 (60) (overall), 8JX8 (61) and EMD-36692 (62) (head), 8JX9 (63) and EMD-36693 (64) (bodyA), 8JXA (65) and EMD-36694 (66) (bodyB), 8JXB (67) and EMD-36695 (68) (wingA), 8JXC (69) and EMD-36696 (70) (wingB), and 8JXD (71) and EMD-36697 (72) (leg), respectively. The coordinates and cryo-EM maps of the rat megalin-RAP complex are deposited with the PDB and EMD codes of 8JUT (73) and EMD-36663 (74) (overall), 8JXE (75) and EMD-36698 (76) (head), 8JXF (77) and EMD-36699 (78) (bodyA), 8JXG (79) and EMD-36700 (80) (bodyB), 8JXH (81) and EMD-36701 (82) (wingA), 8JXI (83) and EMD-36702 (84) (wingB), and 8JXJ (85) and EMD-36703 (86) (leg), respectively.

**ACKNOWLEDGMENTS.** We thank Dr. Yutaka Yoshida for instruction on mass spectrometric analysis; Dr. Yoshinobu Ichimura for SEC; Dr. Yasuyuki Ito for advice on protein purification; Dr. Keitaro Yamashita for assisting structure refinement and modeling; Mr. Youichi Sakamaki, Mr. Toshie Furuya, Mr. Ryota Kobayashi, Ms. Nanako Sugita, Ms. Taeko Endo, and Dr. Hiroyuki Aoki for technical assistance; and Denka Co., Ltd. for preparing the monoclonal anti-megalin antibodies. This research was supported by grants from the Japan Society for the Promotion of Science KAKENHI (20H03216 and 23H02439 to Prof. Nishizawa and JP21H02934 to Prof. Saito), the Practical Research Project for Renal Diseases of the Japan Agency for Medical Research and Development (AMED) (JP19ek0310014, JP20ek0310014, JP21ek0310014, JP22ek0310019, and JP23ek0310019), and the Platform Project for Supporting Drug Discovery and Life Science Research (Basis for Supporting Innovative Drug Discovery and Life Science Research) of AMED (22ama121002 and 22ama121033).

Author affiliations: <sup>a</sup>Department of Applied Molecular Medicine, Kidney Research Center, Niigata University Graduate School of Medical and Dental Sciences, Niigata City 951-8510, Japan; <sup>b</sup>Department of Cell Biology and Anatomy, Graduate School of Medicine, The University of Tokyo, Tokyo 113-0033, Japan; <sup>c</sup>Department of the Biological Membrane Dynamics, Graduate School of Medical Life Science, Yokohama City University, Yokohama 230-0045, Japan; <sup>d</sup>Department of Clinical Nutrition Science, Kidney Research Center, Niigata University Graduate School of Medical and Dental Sciences, Niigata City 951-8510, Japan; <sup>e</sup>Medical Device Development and Regulation Research Center, School of Engineering, The University of Tokyo, Tokyo 113-8656, Japan; and <sup>f</sup>Department of Bioengineering, School of Engineering, The University of Tokyo, Tokyo 113-8656, Japan

Author contributions: A.S. designed research; S.G., A.T., Y.L., K.K., S.N., K. Takemoto, and T.N. performed research; S.G., A.T., Y.L., S.N., K. Tsumoto, T.N., M.K., and A.S. analyzed data; and S.G., M.H., H.K., T.N., M.K., and A.S. wrote the paper.

1. R. Irannejad, N. G. Tsvetanova, B. T. Lobingier, M. von Zastrow, Effects of endocytosis on receptor-mediated signaling. *Curr. Opin. Cell Biol.* **35**, 137–143 (2015).
2. M. L. Eshbach, O. A. Weisz, Receptor-mediated endocytosis in the proximal tubule. *Annu. Rev. Physiol.* **79**, 425–448 (2017).
3. T. E. Willnow, A. Nykjaer, Cellular uptake of steroid carrier proteins—mechanisms and implications. *Mol. Cell Endocrinol.* **316**, 93–102 (2010).
4. A. Saito, S. Pietromonaco, A. K. Loo, M. G. Farquhar, Complete cloning and sequencing of rat gp330/megalin, a distinctive member of the low density lipoprotein receptor gene family. *Proc. Natl. Acad. Sci. U.S.A.* **91**, 9725–9729 (1994).
5. J. Yochem, I. Greenwald, A gene for a low density lipoprotein receptor-related protein in the nematode *Caenorhabditis elegans*. *Proc. Natl. Acad. Sci. U.S.A.* **90**, 4572–4576 (1993).
6. E. I. Christensen, H. Birn, T. Storm, K. Weyer, R. Nielsen, Endocytic receptors in the renal proximal tubule. *Physiology (Bethesda)* **27**, 223–236 (2012).
7. E. I. Christensen *et al.*, Segmental distribution of the endocytosis receptor gp330 in renal proximal tubules. *Eur. J. Cell Biol.* **66**, 349–364 (1995).
8. E. I. Christensen, P. J. Verroust, Megalin and cubilin, role in proximal tubule function and during development. *Pediatr. Nephrol.* **17**, 993–999 (2002).
9. S. Kantarci *et al.*, Mutations in LRP2, which encodes the multiligand receptor megalin, cause Donnai-Barrow and facio-oculo-acoustico-renal syndromes. *Nat. Genet.* **39**, 957–959 (2007).
10. Y. Hori *et al.*, Megalin blockade with cilastatin suppresses drug-induced nephrotoxicity. *J. Am. Soc. Nephrol.* **28**, 1783–1791 (2017).
11. J. Kim, A. J. Ricci, In vivo real-time imaging reveals megalin as the aminoglycoside gentamicin transporter into cochlea whose inhibition is otoprotective. *Proc. Natl. Acad. Sci. U.S.A.* **119**, e2117946119 (2022).
12. B. V. Zlokovic *et al.*, Glycoprotein 330/megalin: Probable role in receptor-mediated transport of apolipoprotein J alone and in a complex with Alzheimer disease amyloid beta at the blood-brain and blood-cerebrospinal fluid barriers. *Proc. Natl. Acad. Sci. U.S.A.* **93**, 4229–4234 (1996).
13. A. Beenken *et al.*, Structures of LRP2 reveal a molecular machine for endocytosis. *Cell* **186**, 821–836.e13 (2023).
14. R. Dagil, C. O'Shea, A. Nykjaer, A. M. Bonvin, B. B. Kragelund, Gentamicin binds to the megalin receptor as a competitive inhibitor using the common ligand binding motif of complement type repeats: Insight from the nmr structure of the 10th complement type repeat domain alone and in complex with gentamicin. *J. Biol. Chem.* **288**, 4424–4435 (2013).
15. T. E. Willnow *et al.*, Defective forebrain development in mice lacking gp330/megalin. *Proc. Natl. Acad. Sci. U.S.A.* **93**, 8460–8464 (1996).
16. A. Sato, Y. Shimada, J. Herz, T. Yamamoto, H. Jingami, 39-kDa receptor-associated protein (RAP) facilitates secretion and ligand binding of extracellular region of very-low-density-lipoprotein receptor: Implications for a distinct pathway from low-density-lipoprotein receptor. *Biochem. J.* **341**, 377–383 (1999).
17. D. Biemesderfer, G. Dekan, P. S. Aronson, M. G. Farquhar, Biosynthesis of the gp330/44-kDa Heymann nephritis antigenic complex: Assembly takes place in the ER. *Am. J. Physiol.* **264**, F1011–F1020 (1993).
18. H. Birn, H. Vorum, P. J. Verroust, S. K. Moestrup, E. I. Christensen, Receptor-associated protein is important for normal processing of megalin in kidney proximal tubules. *J. Am. Soc. Nephrol.* **11**, 191–202 (2000).
19. C. B. Andersen, S. K. Moestrup, How calcium makes endocytic receptors attractive. *Trends Biochem. Sci.* **39**, 82–90 (2014).
20. R. P. Czekay, R. A. Orlando, L. Woodward, M. Lundstrom, M. G. Farquhar, Endocytic trafficking of megalin/RAP complexes: Dissociation of the complexes in late endosomes. *Mol. Biol. Cell* **8**, 517–532 (1997).
21. J. Jumper *et al.*, Highly accurate protein structure prediction with AlphaFold. *Nature* **596**, 583–589 (2021).
22. W. Morelle *et al.*, Characterization of the N-linked oligosaccharides of megalin (gp330) from rat kidney. *Glycobiology* **10**, 295–304 (2000).
23. G. A. Jensen *et al.*, Binding site structure of one LRP-RAP complex: Implications for a common ligand-receptor binding motif. *J. Mol. Biol.* **362**, 700–716 (2006).
24. D. Fass *et al.*, Structure of a murine leukemia virus receptor-binding glycoprotein at 2.0 angstrom resolution. *Science* **277**, 1662–1666 (1997).
25. M. Marino, D. Andrews, D. Brown, C. R. Mc, Transcytosis of retinol-binding protein across renal proximal tubule cells after megalin (gp 330)-mediated endocytosis. *J. Am. Soc. Nephrol.* **12**, 637–648 (2001).
26. J. Gburek *et al.*, Megalin and cubilin are endocytic receptors involved in renal clearance of hemoglobin. *J. Am. Soc. Nephrol.* **13**, 423–430 (2002).
27. R. A. Orlando *et al.*, Identification of the second cluster of ligand-binding repeats in megalin as a site for receptor-ligand interactions. *Proc. Natl. Acad. Sci. U.S.A.* **94**, 2368–2373 (1997).
28. J. E. Croy, W. D. Shin, M. F. Knauer, D. J. Knauer, E. A. Komives, All three LDL receptor homology regions of the LDL receptor-related protein bind multiple ligands. *Biochemistry* **42**, 13049–13057 (2003).
29. Z. Cheng *et al.*, Crystal structures of the extracellular domain of LRP6 and its complex with DKK1. *Nat. Struct. Mol. Biol.* **18**, 1204–1210 (2011).
30. J. Kim *et al.*, Sclerostin inhibits Wnt signaling through tandem interaction with two LRP6 ectodomains. *Nat. Commun.* **11**, 5357 (2020).
31. J. Takagi, Y. Yang, J. H. Liu, J. H. Wang, T. A. Springer, Complex between nidogen and laminin fragments reveals a paradigmatic beta-propeller interface. *Nature* **424**, 969–974 (2003).
32. S. Wang *et al.*, Site-specific O-glycosylation of members of the low-density lipoprotein receptor superfamily enhances ligand interactions. *J. Biol. Chem.* **293**, 7408–7422 (2018).
33. E. Tian *et al.*, Galnt11 regulates kidney function by glycosylating the endocytosis receptor megalin to modulate ligand binding. *Proc. Natl. Acad. Sci. U.S.A.* **116**, 25196–25202 (2019).

34. M. G. Farquhar, A. Saito, D. Kerjaschki, R. A. Orlando, The Heymann nephritis antigenic complex: Megalin (gp330) and RAP. *J. Am. Soc. Nephrol.* **6**, 35–47 (1995).
35. J. Herz, J. L. Goldstein, D. K. Strickland, Y. K. Ho, M. S. Brown, 39-kDa protein modulates binding of ligands to low density lipoprotein receptor-related protein/alpha 2-macroglobulin receptor. *J. Biol. Chem.* **266**, 21232–21238 (1991).
36. T. E. Willnow, J. L. Goldstein, K. Orth, M. S. Brown, J. Herz, Low density lipoprotein receptor-related protein and gp330 bind similar ligands, including plasminogen activator-inhibitor complexes and lactoferrin, an inhibitor of chylomicron remnant clearance. *J. Biol. Chem.* **267**, 26172–26180 (1992).
37. M. Z. Kounnas, D. A. Chappell, D. K. Strickland, W. S. Argraves, Glycoprotein 330, a member of the low density lipoprotein receptor family, binds lipoprotein lipase in vitro. *J. Biol. Chem.* **268**, 14176–14181 (1993).
38. E. I. Christensen, J. Gliemann, S. K. Moestrup, Renal tubule gp330 is a calcium binding receptor for endocytic uptake of protein. *J. Histochem. Cytochem.* **40**, 1481–1490 (1992).
39. G. Bu, M. P. Marzolo, Role of rap in the biogenesis of lipoprotein receptors. *Trends Cardiovasc. Med.* **10**, 148–155 (2000).
40. J. Hilpert *et al.*, Megalin antagonizes activation of the parathyroid hormone receptor. *J. Biol. Chem.* **274**, 5620–5625 (1999).
41. R. Gonzalez-Villalobos, R. B. Klassen, P. L. Allen, L. G. Navar, T. G. Hammond, Megalin binds and internalizes angiotensin II. *Am. J. Physiol. Renal Physiol.* **288**, F420–F427 (2005).
42. R. Gonzalez-Villalobos *et al.*, Megalin binds and internalizes angiotensin-(1–7). *Am. J. Physiol. Renal Physiol.* **290**, F1270–F1275 (2006).
43. M. Simonovic *et al.*, Calcium coordination and pH dependence of the calcium affinity of ligand-binding repeat CR7 from the LRP. Comparison with related domains from the LRP and the LDL receptor. *Biochemistry* **40**, 15127–15134 (2001).
44. F. R. Maxfield, D. J. Yamashiro, Endosome acidification and the pathways of receptor-mediated endocytosis. *Adv. Exp. Med. Biol.* **225**, 189–198 (1987).
45. S. Goto *et al.*, Megalin is involved in angiotensinogen-induced, angiotensin II-mediated ERK1/2 signaling to activate Na<sup>+</sup>-H<sup>+</sup> exchanger 3 in proximal tubules. *J. Hypertens* **41**, 1831–1843 (2023), 10.1097/HJH.0000000000003555.
46. M. Hosojima *et al.*, Regulation of megalin expression in cultured proximal tubule cells by angiotensin II type 1A receptor- and insulin-mediated signaling cross talk. *Endocrinology* **150**, 871–878 (2009).
47. S. Ogasawara *et al.*, Significance of urinary full-length and ectodomain forms of megalin in patients with type 2 diabetes. *Diabetes Care* **35**, 1112–1118 (2012).
48. A. Kawasaki *et al.*, Growth cone phosphoproteomics reveals that GAP-43 phosphorylated by JNK is a marker of axon growth and regeneration. *iScience* **4**, 190–203 (2018).
49. A. C. Paoletti *et al.*, Quantitative proteomic analysis of distinct mammalian Mediator complexes using normalized spectral abundance factors. *Proc. Natl. Acad. Sci. U.S.A.* **103**, 18928–18933 (2006).
50. D. N. Mastrorade, Automated electron microscope tomography using robust prediction of specimen movements. *J. Struct. Biol.* **152**, 36–51 (2005).
51. J. Zivanov, T. Nakane, S. H. W. Scheres, Estimation of high-order aberrations and anisotropic magnification from cryo-EM data sets in RELION-3.1. *IUCr* **7**, 253–267 (2020).
52. T. Bepler *et al.*, Positive-unlabeled convolutional neural networks for particle picking in cryo-electron micrographs. *Nat. Methods* **16**, 1153–1160 (2019).
53. P. Emsley, K. Cowtan, Coot: Model-building tools for molecular graphics. *Acta Crystallogr. D Biol. Crystallogr.* **60**, 2126–2132 (2004).
54. T. I. Croll, ISOLDE: A physically realistic environment for model building into low-resolution electron-density maps. *Acta Crystallogr. D Struct. Biol.* **74**, 519–530 (2018).
55. E. F. Pettersen *et al.*, UCSF ChimeraX: Structure visualization for researchers, educators, and developers. *Protein Sci.* **30**, 70–82 (2021).
56. D. Liebschner *et al.*, Macromolecular structure determination using X-rays, neutrons and electrons: Recent developments in Phenix. *Acta Crystallogr. D Struct. Biol.* **75**, 861–877 (2019).
57. K. Yamashita, C. M. Palmer, T. Burnley, G. N. Murshudov, Cryo-EM single-particle structure refinement and map calculation using Servalcat. *Acta Crystallogr. D Struct. Biol.* **77**, 1282–1291 (2021).
58. S. Goto, A. Saito, Mass spectrometric analysis of purified megalin. jPOST. <https://repository.jpostdb.org/entry/JPST001959>. Deposited 16 December 2022.
59. S. Goto *et al.*, Rat megalin. PDB. <https://www.rcsb.org/structure/8JUJ>. Deposited 27 June 2023.
60. S. Goto *et al.*, Rat megalin. EMD. <https://www.ebi.ac.uk/emdb/EMD-36664>. Deposited 27 June 2023.
61. S. Goto *et al.*, Rat megalin head. PDB. <https://www.rcsb.org/structure/8JX8>. Deposited 30 June 2023.
62. S. Goto *et al.*, Rat megalin head. EMD. <https://www.ebi.ac.uk/emdb/EMD-36692>. Deposited 30 June 2023.
63. S. Goto *et al.*, Rat megalin bodyA. PDB. <https://www.rcsb.org/structure/8JX9>. Deposited 30 June 2023.
64. S. Goto *et al.*, Rat megalin bodyA. EMD. <https://www.ebi.ac.uk/emdb/EMD-36693>. Deposited 30 June 2023.
65. S. Goto *et al.*, Rat megalin bodyB. PDB. <https://www.rcsb.org/structure/8JXA>. Deposited 30 June 2023.
66. S. Goto *et al.*, Rat megalin bodyB. EMD. <https://www.ebi.ac.uk/emdb/EMD-36694>. Deposited 30 June 2023.
67. S. Goto *et al.*, Rat megalin wingA. PDB. <https://www.rcsb.org/structure/8JXB>. Deposited 30 June 2023.
68. S. Goto *et al.*, Rat megalin wingA. EMD. <https://www.ebi.ac.uk/emdb/EMD-36695>. Deposited 30 June 2023.
69. S. Goto *et al.*, Rat megalin wingB. PDB. <https://www.rcsb.org/structure/8JXC>. Deposited 30 June 2023.
70. S. Goto *et al.*, Rat megalin wingB. EMD. <https://www.ebi.ac.uk/emdb/EMD-36696>. Deposited 30 June 2023.
71. S. Goto *et al.*, Rat megalin leg. PDB. <https://www.rcsb.org/structure/8JXD>. Deposited 30 June 2023.
72. S. Goto *et al.*, Rat megalin leg. EMD. <https://www.ebi.ac.uk/emdb/EMD-36697>. Deposited 30 June 2023.
73. S. Goto *et al.*, Rat megalin RAP complex. PDB. <https://www.rcsb.org/structure/8JUT>. Deposited 30 June 2023.
74. S. Goto *et al.*, Rat megalin RAP complex. EMD. <https://www.ebi.ac.uk/emdb/EMD-36663>. Deposited 30 June 2023.
75. S. Goto *et al.*, Rat megalin RAP complex head. PDB. <https://www.rcsb.org/structure/8JXE>. Deposited 30 June 2023.
76. S. Goto *et al.*, Rat megalin RAP complex head. EMD. <https://www.ebi.ac.uk/emdb/EMD-36698>. Deposited 30 June 2023.
77. S. Goto *et al.*, Rat megalin RAP complex bodyA. PDB. <https://www.rcsb.org/structure/8JXF>. Deposited 30 June 2023.
78. S. Goto *et al.*, Rat megalin RAP complex bodyA. EMD. <https://www.ebi.ac.uk/emdb/EMD-36699>. Deposited 30 June 2023.
79. S. Goto *et al.*, Rat megalin RAP complex bodyB. PDB. <https://www.rcsb.org/structure/8JXG>. Deposited 30 June 2023.
80. S. Goto *et al.*, Rat megalin RAP complex bodyB. EMD. <https://www.ebi.ac.uk/emdb/EMD-36700>. Deposited 30 June 2023.
81. S. Goto *et al.*, Rat megalin RAP complex wingA. PDB. <https://www.rcsb.org/structure/8JXH>. Deposited 30 June 2023.
82. S. Goto *et al.*, Rat megalin RAP complex wingA. EMD. <https://www.ebi.ac.uk/emdb/EMD-36701>. Deposited 30 June 2023.
83. S. Goto *et al.*, Rat megalin RAP complex wingB. PDB. <https://www.rcsb.org/structure/8JXI>. Deposited 30 June 2023.
84. S. Goto *et al.*, Rat megalin RAP complex wingB. EMD. <https://www.ebi.ac.uk/emdb/EMD-36702>. Deposited 30 June 2023.
85. S. Goto *et al.*, Rat megalin RAP complex leg. PDB. <https://www.rcsb.org/structure/8JXJ>. Deposited 30 June 2023.
86. S. Goto *et al.*, Rat megalin RAP complex leg. EMD. <https://www.ebi.ac.uk/emdb/EMD-36703>. Deposited 30 June 2023.